Applied Materials Today 39 (2024) 102347

Contents lists available at ScienceDirect

Applied Materials Today

journal homepage: www.elsevier.com/locate/apmt

Ultrastrong and ductile NiTi-based composite with large recoverable strain mediated by a compositionally complex phase

Jiayi Geng [a,d], Yunzhu Shi [a,*], Pere Barriobero-Vila [b,c], Meiyuan Jiao [e], Yihuan Cao [e], Yu Tang [f], Jingzhi He [f], Chao Ma [a], Yan Ma [g], Zhifeng Lei [a,*], Zhaoping Lu [e,*]

[a] College of Materials Science and Engineering, Hunan University, Changsha, 410082, PR China
[b] Department of Materials Science and Engineering, Technical University of Catalonia (UPC), Barcelona 08019, Spain
[c] CIM, Technical University of Catalonia (UPC), Barcelona 08028, Spain
[d] State Key Laboratory of High-Performance Ceramics and Superfine Microstructure, Shanghai Institute of Ceramics, Chinese Academy of Sciences, Shanghai, 200050, PR China
[e] Beijing Advanced Innovation Center for Materials Genome Engineering, State Key Laboratory for Advanced Metals and Materials, University of Science and Technology Beijing, Beijing 100083, PR China
[f] College of Aerospace Science and Engineering, National University of Defense Technology, Changsha 410073, PR China
[g] Max-Planck-Institut für Eisenforschung, Max-Planck-Straße 1, 40237 Düsseldorf, Germany

ARTICLE INFO

Keywords:
NiTi-based composites
High-entropy alloys
Mechanical properties
Recoverable strain
Phase transformation

ABSTRACT

NiTi-based composites possess great potential for concurrently improving both mechanical and functional properties. However, relying on traditional alloy design principles limits the design space and greatly hinders the advancement of high-performance NiTi-based composites. The concept of high-entropy alloys has expanded the compositional landscape, unveiling unique structural characteristics for alloy design and providing new prospects for addressing these limitations. Here, we report a compositionally complex NiTi-based composite that exhibits exceptional strength and ductility, along with remarkable recoverable strain. The composite, $Ni_{40}Ti_{40}(NbMoTaW)_{20}$ (at.%), comprises a 78.0 % B2 NiTi matrix, a 19.2 % Nb-Mo-Ta-W-Ti-Ni compositionally complex body-centered cubic (BCC) phase, and a small amount of Ti_2Ni. Notably, this composite demonstrates an engineering compressive strength of 3274 MPa, with a compressive fracture strain of 44.2 % and a maximum recoverable strain of 7.3 % (5.6 % elastic strain and 1.7 % inelastic recoverable strain). These outstanding mechanical properties result from the unique structural characteristics of the compositionally complex phase and the lattice strain matching induced by phase transitions. The substantial recoverable strain was obtained through the reversible B2⇌R⇌B19′ phase transition. This work not only innovates a new category of high-performance NiTi-based composites but also extends the applicability of the high-entropy concept.

1. Introduction

Shape memory alloys fall within the category of smart materials, owing to their remarkable capability to undergo substantial reversible phase transformations that define their functional properties [1–3]. Among commercially available shape memory alloys, NiTi alloys are the most widely used due to their exceptional shape memory effect, pseudoelasticity, strong corrosion resistance, biocompatibility, and good processability [4–6]. To cope with the increasingly challenging and intricate service environment, expanding the range of engineering applications of NiTi alloys primarily involves improving their mechanical properties and functional capabilities. To meet this demand, NiTi-based composites, such as NiTi-metal and NiTi-intermetallic compound composites, have become widely adopted solutions. NiTi-Nb [1], NiTi-W [7], NiTi-V [8], NiTi-NbTi [9], NiTi-Ti_3Sn [5], NiTi-Ti_5Si_3 [10] and NiTi-Nb_3Sn [11]. Of particular note is the NiTi-Nb composite, which has a substantial quasi-linear elastic strain of over 6 % and an impressive yield strength of 1.65 GPa [1]. However, conventional design principles restrict the composition range of NiTi-based metallic composites, hindering their further development and performance optimization. Moreover, traditional NiTi-based composites are usually soft due to occurrence of martensitic transformation. Intermetallic compounds are rigid and brittle, which hinders the enhancement of ductility and recoverable strain in NiTi-intermetallic compound composites.

* Corresponding authors.
E-mail addresses: yzshi@hnu.edu.cn (Y. Shi), zflei@hnu.edu.cn (Z. Lei), luzp@ustb.edu.cn (Z. Lu).

https://doi.org/10.1016/j.apmt.2024.102347
Received 17 April 2024; Received in revised form 26 June 2024; Accepted 17 July 2024
Available online 23 July 2024

Therefore, developing innovative NiTi-based composites is imperative to tackle these challenges.

The alloy design concept of high-entropy alloys (HEAs) composed of multiple principal components is a promising solution to address these challenges. The strong configuration entropy effect inherent in HEAs allows for a considerably wide range of compositions in alloy design [12–14]. This compositional diversity endows HEAs with great potential to integrate various performance attributes [15]. Moreover, the variations in atomic size and chemistry among the multiple constituents lead to large lattice distortion. This phenomenon serves to impede dislocation movement, thereby substantially enhancing the strength of HEAs [16–20]. In addition, the complex short-range ordering within these solid solutions enriches their plastic deformation mechanisms, thereby improving their ductility [21–26]. Therefore, utilizing the concept of HEAs reveals captivating opportunities for advancing NiTi-based composites.

Stimulated by the field of HEAs, here, we developed a NiTi-based composite featuring a compositionally complex body-centered cubic (BCC) phase embedded in a B2 NiTi matrix. This composite achieves remarkable strength, ductility, and significant recoverable strain. The current findings not only introduce a new class of NiTi-based composites for engineering applications, but also offer insights into the design of innovative multifunctional metallic materials using the HEA concept.

2. Materials and methods

2.1. Material preparation

Alloy ingots with a nominal composition of $Ni_{40}Ti_{40}(NbMoTaW)_{20}$ (at.%) were prepared by arc melting a mixture of pure metals (purity, >99.9 wt.%) in a Ti-gettered high-purity argon atmosphere. The ingots were remelted at least eight times to ensure chemical homogeneity, and then drop-cast into a water-cooled copper mold with a dimension of $10\times10\times60$ mm^3.

2.2. Mechanical measurements

Compression and cyclic compression tests were conducted at room temperature using an electric universal material testing machine (AGS-X-50KN) with a loading/unloading rate of 1×10^{-3} s^{-1}. The sample size is Φ4 mm × 6 mm. At least five samples were tested. In the loading-unloading tests, cyclic compression strains increased in 3 % increments, starting at 3 %, and continued until reaching failure.

2.3. Microstructural characterization

Microstructure and morphology were characterized by MIRA3 LMU scanning electron microscope (SEM, TESCAN company) operating at 20 kV. The energy-dispersive X-ray spectroscopy (EDS) was utilized to analyze the elemental distribution. The area fraction of each phase was calculated and measured by ImageJ software. The SEM sample was initially polished with 2000-grit SiC paper. Then, the sample was mechanically polished with a diamond plaster in a metallographic polishing machine (LMD-2C). Subsequently, the sample was polished with a colloidal silica suspension in a vibratory polishing machine (Vibra 304). Transmission electron microscopy (TEM, FEI Talos F200X) operating at 200 kV. The TEM sample was mechanically ground to a thickness of 50 μm and then twin-jet electropolished using 10% sulfuric acid + 90% methanol (vol.%) solution under a temperature of −20 °C, a voltage of 15 V. Phase transformation behavior of the composite was studied through differential scanning calorimetry (DSC) using a TA DSC25 unit at a cooling/heating rate of 10 K/min in a nitrogen atmosphere.

2.4. In-situ synchrotron high-energy X-ray diffraction

In-situ high-energy X-ray diffraction (XRD) during compression was carried out at the beamline P07-HEMS of PETRA III, Deutsches Elektronen-Synchrotron (DESY) [27]. Uniaxial compression was performed at room temperature (RT) using a modified dilatometer Bähr 805A/D equipped with a deformation unit [28]. Sequences of entire Debye-Scherrer rings were recorded from the bulk material in transmission mode using a Perkin Elmer XRD 1621 image-plate detector. The incident X-ray beam (perpendicular to the loading direction) was positioned at the center of the sample's length. A slit size of 0.8×0.8 mm^2 resulting in a gage volume of $0.8 \times 0.8 \times 4$ mm^3 was used. The sample-detector distance and acquisition time were 1600 mm and 1 s, respectively. An illustrative diagram of the experimental setup is presented in ref. [29]. The beam energy was 100 keV (wavelength = 0.124 Å). The instrument parameters were calibrated using a LaB6 powder standard. One-dimensional (1-D) high-energy XRD patterns were obtained by integrating across all angles in the 2-D diffraction patterns under various applied strains (**Supplementary Figure 1**). The lattice strain under various applied strains was fitted by distorting two-dimensional (2-D) diffraction patterns using GSAS-II software package [30]. The lattice strain for a specific set of crystal planes was calculated as $|d_{hkl} - d^0_{hkl}|/d^0_{hkl}$, where d^0_{hkl} represents the d-spacing in the unloaded condition. Positive for compression and negative for tension in the direction of loading.

3. Results and discussion

3.1. Mechanical and superelastic properties

Fig. 1a illustrates the compressive engineering stress-strain curve of the $Ni_{40}Ti_{40}(NbMoTaW)_{20}$ composite, revealing a prominent double-yielding phenomenon. Stress-induced martensitic transformation of the B2 NiTi phase within the composite contributes to the first yielding [31]. The first yield stress σ_{FY} and strain ε_{FY} are 469 ± 24 MPa and 2.87 % ± 0.16 %, respectively, whilest the second yield stress σ_{SY} and strain ε_{SY} are 1089 ± 30 MPa and 11.34 ± 0.55 %, respectively. The ultimate strength σ_{US} and fracture strain ε_{FS} are significantly increased to 3274 ± 56 MPa and 44.2 % ± 0.2 %, respectively. **Supplementary Figure 2** presents the fracture morphology of the composite, showing pronounced ductile tearing and a large number of dimples in $Ni_{40}Ti_{40}(NbMoTaW)_{20}$, indicative of its superior ductility. Fig. 1b shows a plot of the ultimate strength against fracture strain for the current $Ni_{40}Ti_{40}(NbMoTaW)_{20}$, and previously reported NiTi-based alloys and composites [11,32–49]. It is worth noting that we focus solely on conventional bulk samples and exclude wire samples from the analysis. For comparison, compressive mechanical properties of the $Ni_{40}Ti_{40}Nb_{20}$ composite were also examined (**Supplementary Figure 3**). The $Ni_{40}Ti_{40}(NbMoTaW)_{20}$ composite exhibits high strength and large ductility. In addition, the composite features a low Young's modulus of 17.9 ± 0.9 GPa, enabling significant elastic strain under low stress conditions and potentially enhancing its superelastic performance.

Fig. 1c depicts the compressive cyclic stress-strain curve of $Ni_{40}Ti_{40}(NbMoTaW)_{20}$. Notably, during cyclic loading, the ultimate strength and fracture strain of the composite are consistent with those under continuous loading (Fig. 1a). By analyzing the cyclic stress-strain curve, we calculated the superelastic strain ε_{SE} and recoverable strain ε_{RS} of the composite (**Supplementary Figure 4**). Initially, the superelastic strain ε_{SE}, induced by the reversed martensite to austenite phase transformation, increases during the first three cycles (ε<9 %) and stabilizes at approximately 1.5 % (see the lower part of **Supplementary Figure 4b**). In contrast, the recoverable strain ε_{RS} of the composite increases with cyclic loading. The recoverable strain climbs from 2.1 % to 7.3 % under cyclic loading (see the upper part of **Supplementary Figure 4b**). Thus, $Ni_{40}Ti_{40}(NbMoTaW)_{20}$ exhibits not only superb mechanical properties but also attractive superelastic characteristics. Fig. 1d compares the superelastic properties of $Ni_{40}Ti_{40}(NbMoTaW)_{20}$ with the $Ni_{40}Ti_{40}Nb_{20}$ composite (**Supplementary Figure 5**) and other

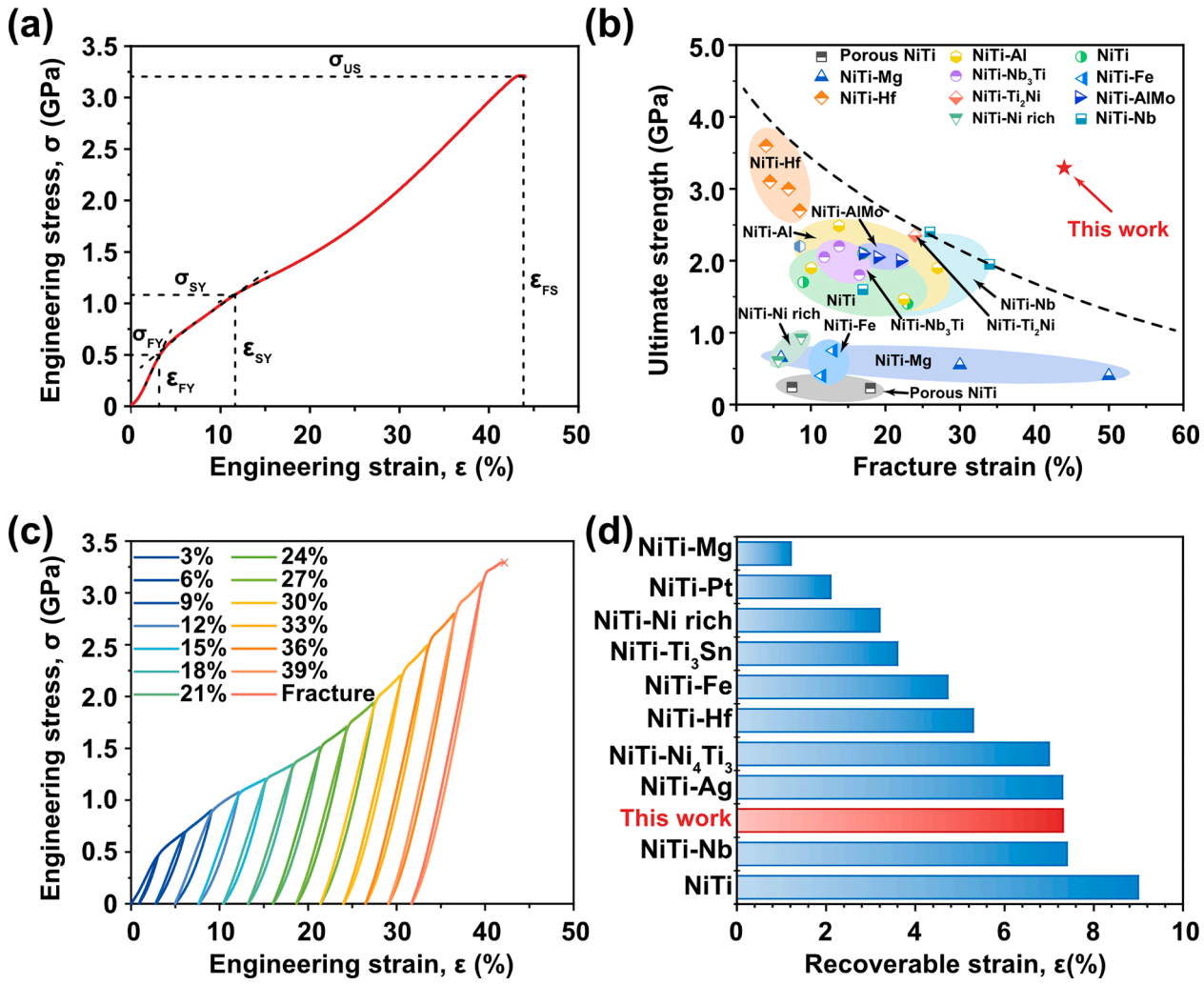

Fig. 1. Mechanical and superelastic properties. (a) Compressive engineering stress-strain curve of the $Ni_{40}Ti_{40}(NbMoTaW)_{20}$ composite. Key points on the stress-strain curve are labeled as follows: σ_{FY}: the first yield stress, ε_{FY}: the first yield strain, σ_{SY}: the second yield stress, ε_{SY}: the second yield strain, σ_{US}: the ultimate strength, ε_{FS}: fracture strain. **(b)** Ultimate strength versus fracture strain of the $Ni_{40}Ti_{40}(NbMoTaW)_{20}$ composite in comparison with NiTi and other NiTi-based composites [11,32–49]. (c) Engineering stress-strain curve during cyclic compression for the $Ni_{40}Ti_{40}(NbMoTaW)_{20}$ composite. During the loading-unloading test, the cyclic compression strains range from 3 %, 6 %, 9 %, 12 %, and so forth until failure occurs. **(d)** Recoverable strain of the $Ni_{40}Ti_{40}(NbMoTaW)_{20}$ composite in comparison with NiTi and other NiTi-based composites [1,32,34,39,40,43,46–57].

NiTi-based alloys/composites [1,32,34,39,40,43,46–57]. As shown, $Ni_{40}Ti_{40}(NbMoTaW)_{20}$ shows a maximum recoverable strain comparable to NiTi-Nb and NiTi-Ag composites, underscoring its superior superelastic features.

3.2. *Microstructure characterization*

To unveil the intrinsic mechanisms governing the mechanical and superelastic properties of this material, we meticulously examined its phase constitutions. Fig. 2a displays the high-energy X-ray diffraction (XRD) pattern of $Ni_{40}Ti_{40}(NbMoTaW)_{20}$. The composite primarily consists of B2 and BCC phases, accompanied by a limited quantity of Ti_2Ni and R phases. Accordingly, the lattice constant is 3.024 Å for the B2 phase and 3.200 Å for the BCC phase (see **Supplementary Figure 6**). The lattice misfit between the B2 NiTi and BCC phases is 5.5 %, which is lower than that in typical NiTi-Nb composites. This facilitates achieving lattice strain matching. The B2→R transition induces less crystallographic distortion compared to the B2→B19′ transition. This smoother transition in the B2 phase reduces localized stresses from the phase transition, thereby potentially minimizing defect generation.

Fig. 2b captures a scanning electron microscope (SEM) micrograph of the $Ni_{40}Ti_{40}(NbMoTaW)_{20}$ composite, unveiling a microstructure characterized by large white particles dispersed throughout the matrix. After careful examination, white strips are observed decorating the grain boundaries, with a small number of black strips located at the junctions of the mesh-like white strips (Fig. 2c). The corresponding energy-dispersive X-ray spectroscopy (EDS) results reveal that Ni and Ti elements are enriched in the matrix, Nb, Mo, Ta, and W elements are enriched in the large white particles and white strips, and Ni and Ti elements are enriched in the black strips (**Supplementary Figure 7**). The detailed compositions for each phase are provided in **Table S1**. In the matrix, the atomic ratio of Ni and Ti elements is close to 1:1, while in the black strips, the ratio tends to be 1:2. Combining the high-energy XRD and SEM results, it was found that the matrix corresponds to the B2 NiTi phase, the black strips is the Ti_2Ni phase, and the white particles and strips are the BCC phase. Specifically, for the BCC phase in $Ni_{40}Ti_{40}(NbMoTaW)_{20}$, the concentration of Ni, Ti, Nb, Mo, Ta and W were measured to be 10.05±2.50 at.%, 19.95±3.84 at.%, 13.96±1.77 at.%, 13.51±0.93 at.%, 18.23±1.36 at.% and 24.29±6.82 at.%, respectively. The BCC phase exhibits an ideal configurational mixing entropy of approximately 14.56 $J{\cdot}mol^{-1}{\cdot}K^{-1}$, well within the range established for HEAs by Yeh et al [58]. The pseudobinary phase diagram

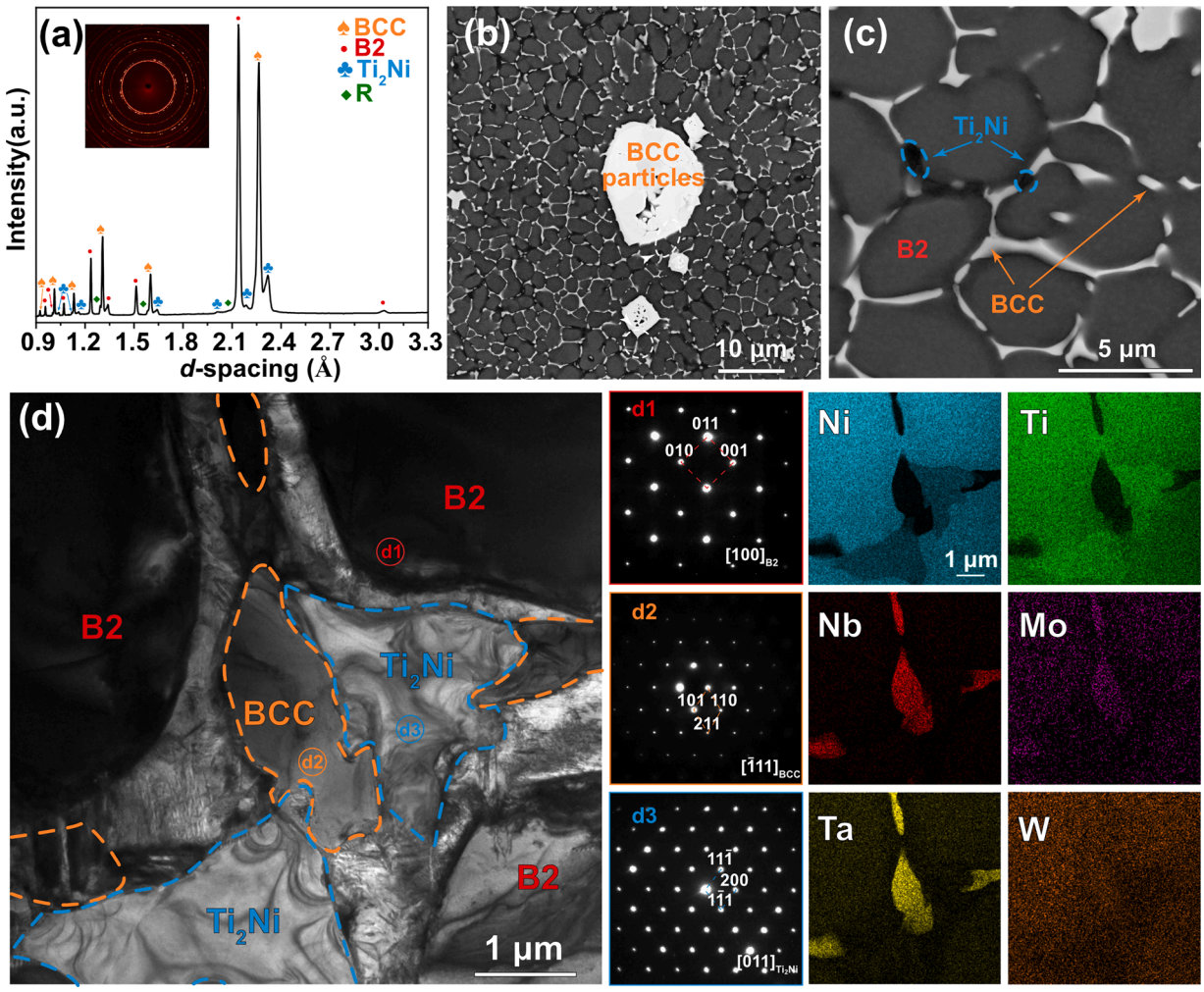

Fig. 2. Microstructure characterization. (a) Synchrotron high-energy X-ray diffraction (XRD) pattern of the $Ni_{40}Ti_{40}(NbMoTaW)_{20}$ composite, with the inset revealing the Debye–Scherrer rings. **(b)** Scanning electron microscope (SEM) image of the $Ni_{40}Ti_{40}(NbMoTaW)_{20}$ composite. **(c)** Corresponding local enlargement of (b). The white arrows highlight the B2 phase and BCC phase coexistenc region, the orange arrows depict the body-centered cubic (BCC) particles and strips, and the blue arrows illustrate the Ti_2Ni strips. **(d)** Bright-field transmission electron microscopy (TEM) image offering a detailed view of the B2 NiTi matrix, BCC phases, and the Ti_2Ni precipitates. **d1, d2** and **d3** are the corresponding selected area electron diffraction pattern of the B2 NiTi, BCC and Ti_2Ni phases. The two columns on the right showcase the elemental distribution mapping, illustrating the spatial distribution of Ni, Ti, Nb, Mo, Ta, and W.

of the NiTi–Nb system shows that a eutectic microstructure forms, comprising B2 NiTi and BCC Nb phases [36]. Mo, Ta, W, and Nb share similar chemistry and can mix infinitely. Substituting Nb with (Nb, Mo, Ta, W) in the NiTi-based composite enhances mixing entropy, stabilizing the BCC phase. Moreover, the area fractions of the B2, BCC, and Ti_2Ni phases were determined to be 78.0 %±4.1 %, 19.2 %±5.3 %, and 2.8 % ±1.6 %, respectively. Therefore, we can classify the current BCC phase as a compositionally complex phase.

To delve into the atomic-scale microstructure features of $Ni_{40}Ti_{40}(NbMoTaW)_{20}$, we utilized transmission electron microscopy (TEM). Fig. 2d shows a representative bright-field TEM image. The selected area electron diffraction (SAED) pattern (**Figures. 2d1-d3)** clearly identifies the matrix as B2, white strips as BCC, and black strips as Ti_2Ni. The B2 and BCC structures were further affirmed through a high-resolution TEM image and the corresponding fast Fourier transformation (FFT) image (**Supplementary Figure 8**). Both distinctly illustrate the ordered atomic arrangement of B2 versus the disordered atomic arrangement of BCC. The corresponding TEM-EDS mapping analysis further demonstrates the enrichment of Nb, Mo, Ta, and W elements in the BCC phase, while Ni and Ti elements dominate the composition of the B2 matrix and Ti_2Ni phase (Fig. 2d). Remarkably, the Ni enrichment in the Ti_2Ni phase is lower than that in the B2 matrix, whereas the Ti enrichment follows an opposite trend. The Ti_2Ni strips exhibit a tendency to connect the BCC phase, forming a continuous mesh-like structure. A similar structure, arising from the partial substitution of Ti atoms by Nb atoms in the B2 phase, has also been observed in NiTi-Nb composites. This phenomenon leads to the accumulation of expelled Ti atoms at grain boundaries, thus resulting in the formation of the Ti_2Ni phase [59]. It is worth noting that other refractory elements may have similar effects.

3.3. Transformation behavior

To comprehend the phase transformation mechanisms in the present $Ni_{40}Ti_{40}(NbMoTaW)_{20}$ composite, we conducted differential scanning calorimetry (DSC) measurement (Fig. 3**a**). In the heating and cooling cycle, the material manifests two exothermic peaks and two endothermic peaks. Microstructure analysis reveals the predominant presence of the B2 NiTi and BCC phases within the composite. Specifically, when doped with additional elements, the B2 NiTi phase typically experiences a two-step phase transition B2⇌R⇌B19′. This dual transformation is characterized by two exothermic peaks and two endothermic peaks [60]. Thus, it can be deduced that the

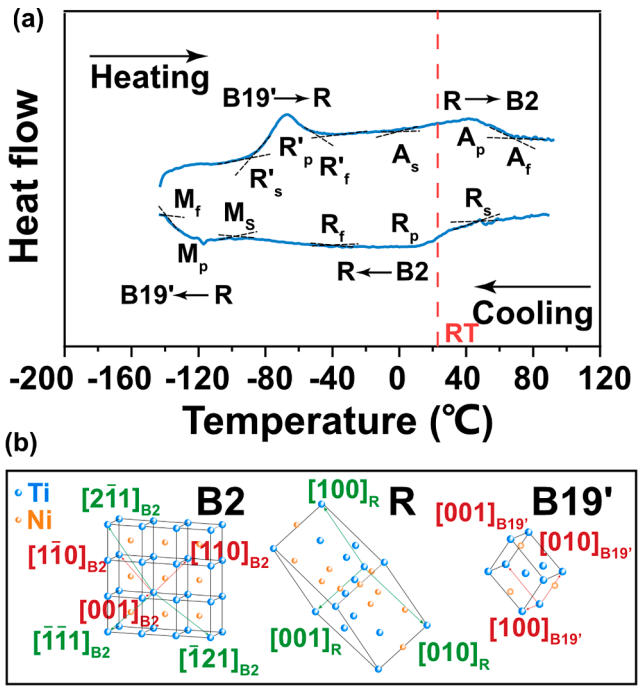

Fig. 3. Transformation behavior. (a) Differential scanning calorimetry (DSC) curve for the $Ni_{40}Ti_{40}(NbMoTaW)_{20}$ composite, providing insights into various transformation temperatures. Key points on the DSC curve are labeled as follows: RT (room temperature), R_s (start temperature of B2→R transition), R_p (peak temperature of B2→R transition), R_f (finish temperature of B2→R transition), M_s (start temperature of R→B19′ martensitic transformation), M_p (peak temperature of R→B19′ martensitic transformation), M_f (finish temperature of R→B19′ martensitic transformation), R'_s (start temperature of B19′→R transition), R'_p (peak temperature of B19′→R transition), R'_f (finish temperature of B19′→R transition), A_s (start temperature of R→B2 austenitic transformation), A_p (peak temperature of R→B2 austenitic transformation), and A_f (finish temperature of R→B2 austenitic transformation). **(b)** Schematic diagram illustrating the interconversion between the B2, R, and B19′ phases.

$Ni_{40}Ti_{40}(NbMoTaW)_{20}$ composite undergoes a two-step B2⇌R⇌B19′ phase transformation during both the cooling and heating cycles. In this case, both the R and B19′ phases undergo diffusionless transformations characterized by minimal displacements. The R phase takes the form of a rhombic structure resulting from the elongation of B2 along the [111] direction, while B19′ adopts a monoclinic structure formed by the displacement of a pair of orthogonal (110) crystal faces in B2 by a certain distance [6,61,62]. Fig. 3**b** illustrates the schematic diagram of the B2 ⇌ R ⇌ B19′ phase transition. During this transition, the transformation relationship of the crystal planes for each phase can be described as:

$(2\bar{1}1)_{B2}\rightleftharpoons(100)_R$;
$(\bar{1}21)_{B2}\rightleftharpoons(010)_R$;
$(\bar{1}\bar{1}1)_{B2}\rightleftharpoons(001)_R$;
$(001)_{B2}\rightleftharpoons(100)_{B19'}$;
$(110)_{B2}\rightleftharpoons(010)_{B19'}$; and
$(1\bar{1}0)_{B2}\rightleftharpoons(001)_{B19'}$.

The occurrence of this two-step transition within the B2 phase in NiTi-based composites is associated with factors such as the introduction of a third element and the ratio of Ni to Ti elements [61,63]. This implies that the inclusion of refractory elements may facilitate the transition from B2 to the R phase. The B2→R transformation start temperature (R_s) and the R→B19′ martensitic transformation start temperature (M_s) are measured at 48.9 °C and −96.1 °C, respectively. The R_s value exceeds room temperature, suggesting the likely presence of the R phase in the $Ni_{40}Ti_{40}(NbMoTaW)_{20}$ composite. This aligns with the high-energy XRD result (Fig. 2a). Also, the low M_s implies a significant difference in chemical potential between B19′ and B2 in $Ni_{40}Ti_{40}(NbMoTaW)_{20}$, potentially yielding a substantial driving force for the reverse transition from B19′ to B2. Moreover, the B19′→R transition finish temperature (R'_f) and the R→B2 austenitic transformation finish temperature (A_f) are measured at −46.5 °C and 71.7 °C, respectively. The low R'_f suggests a thermodynamically favored transition from the B19′ phase to the R phase.

3.4. Deformation processes

To unravel the deformation mechanism exhibited by $Ni_{40}Ti_{40}(NbMoTaW)_{20}$ composite under both continuous and cyclic loading, we conducted *in-situ* synchrotron XRD experiments. Fig. 4a illustrates the continuous loading process. Fig. 4b depicts the *in-situ* synchrotron XRD measurement during continuous loading, revealing a four-stage deformation process. In stage I (macro-strain ε=0–1.8 %), we observe the presence of only the BCC and B2 phases. Notably, their peak positions exhibit subtle leftward shifts, while their peak widths remain largely unaltered. Consequently, this initial stage is primarily characterized by the elastic deformation of the BCC and B2 phases. Moving on to stage II (ε=1.8 %−2.6 %), we observe that the peak positions of the BCC phase continue to shift slightly leftward, indicating that the BCC phase remains in the elastic deformation period. Concurrently, the transition from the B2 phase to the R phase commences, and with further deformation, the emergence of the B19′ phase follows suit (**Supplementary Figure 9**), while the retained B2 phase continues its elastic deformation. The appearance of the B2 → R → B19′ transition during loading demonstrates that the phase transition observed in the DSC measurements is indeed the two-step B2 ⇌ R ⇌ B19′ transition. As we transition into stage III (ε=2.6 %−8.6 %), the B2 phase undergoes a significant transformation into the R phase and subsequently into the B19′ phase. Thus, during this stage, the deformation of the composite is primarily driven by the B2→R→B19′ phase transformation. Stage IV (ε>8.6 %) witnesses the composite mainly comprising the BCC and B19′ phases. Though the peak positions of both phases display minimal changes, the half-peak widths progressively increase with deformation, signifying that this stage is primarily characterized by the plastic deformation of both phases. Fig. 4c illustrates the lattice strain of the BCC and B2 phases during continuous loading. In the elastic strain regime (stage I and II, ε=0–2.6 %), the BCC phase demonstrates a maximum lattice strain of 0.45 %, while the B2 phase undergoes elastic deformation at macro-strain ε of less than 2.6 %. Remarkably, the BCC phase exhibits a substantial elastic strain (ε=2.7 %) during loading, closeing to the onset strain for the B19′ transition (stage II, ε=1.8 %−2.6 %) (Fig. 4d). This phenomenon facilitates a favorable match between the BCC and B2 phases. In the course of the B19′ phase transition (stage III, ε=2.6 %−8.6 %), the lattice strain of the BCC phase increases (Fig. 4c). The slope during this stage is higher than that in the plastic regime (stage IV, ε>8.6 %), indicating the presence of lattice strain and dislocation slip in the BCC phase. Notably, this alignment between the BCC phase and the B19′ phase is achieved primarily through lattice strain rather than dislocation slip, a principle well-documented in studies involving nanowire and shape memory alloy composites, known as the lattice strain matching approach [1,64]. The lattice strain matching approach considerably diminishes the intensity of the elastic strain field at the phase boundary. As we enter stage IV (ε>8.6 %), the lattice strain of the BCC phase gradually increases, with the corresponding slope being lower than that in stage III (ε=2.6 %−8.6 %). This suggests that the BCC phase now predominantly undergoes dislocation slip. The B19′ phase transition primarily occurs in stage III (ε=2.6 %−8.6 %) (Fig. 4d). The fraction of the B19′ phase exhibits a rapid increase with macro-strain, with approximately 75 % of the B2 phase ultimately transforming to the B19′ phase by the end of this stage. In the early period of stage IV (ε=8.6 %−16.7 %), the fraction of the B19′ phase remains relatively constant, possibly owing to the orientation of the B2 phase, which does not favor martensitic phase transformation. However, in the later period (ε>16.7 %), the residual B2 phase initiates

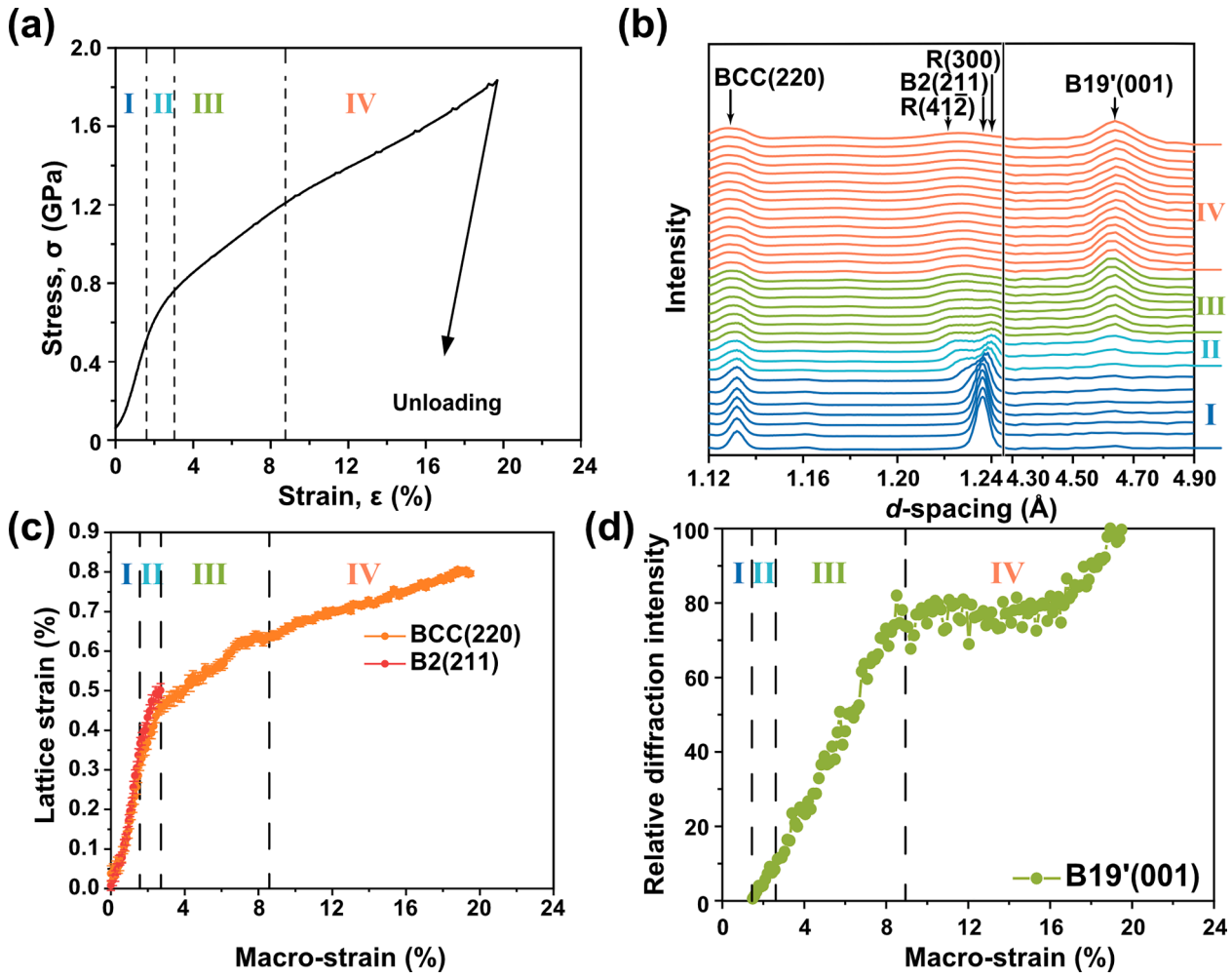

Fig. 4. Deformation mechanisms during continuous loading. (a) Schematic illustration of the continuous loading process. **(b)** *In-situ* synchrotron high-energy X-ray diffraction patterns captured during continuous loading, revealing the dynamic evolution of peaks corresponding to BCC (220), B2 (211), R (41$\bar{2}$), R (300), and B19′ (001). **(c)** The evolution of lattice strain for BCC (220) and B2 (211) planes during continuous loading, with analysis data acquired parallel to the loading direction. **(d)** The evolution of the relative diffraction intensity of B19′ (001) peaks during continuous loading.

transformation into the B19′ phase, suggesting that increased stress and strain trigger the reinitiation of martensitic phase transformation. We also discuss stress transfer during continuous loading (**Supplementary Figure 10**). In stages I and II, the macro-stress versus lattice strain curve for BCC (220) shows a nearly constant slope, indicating elastic deformation of the BCC phase. Stage III exhibits an increased slope, indicating plastic deformation of the BCC phase and stress transfer to the B2 or B19′ phases. In stage IV, the slope continues to increase, demonstrating further stress transfer to the B2 or B19′ phases and additional plastic deformation of the BCC phase.

Fig. 5a depicts the cyclic loading process. Fig. 5b presents the *in-situ* synchrotron XRD measurement under cyclic loading, revealing a distinct reversible B2⇌R⇌B19′ transition. In the initial loading-unloading cycle (O-A-B, ε=0–3 %), the BCC phase peak position shifts leftward during loading (O-A) and then rightward during unloading (A-B). Initially, the half-peak width remains constant until significant broadening close to point A, indicating elastic deformation in the BCC phase, followed by plastic deformation beyond its elastic limit, generating dislocations and peak broadening. The B2 phase transforms to the R phase during loading (O-A) and reverses to the B2 phase during unloading (A-B). The second cycle (B-C-D, ε=1.7 %–6.7 %) sees the BCC phase peak position shift leftward during loading (B-C) and rightward during unloading (C-D). Half-peak width remains initially constant, gradually broadening during loading (indicating elastic and plastic deformation) and remaining constant during unloading. The B2→R→B19′ phase transition occurs during loading (B-C), with the reverse transition during unloading (C-D) (**Supplementary Figure 11**). In the third cycle (D-E-F, ε=4.2 %–18 %), the BCC phase undergoes elastic and plastic deformation during loading (D-E) and primarily elastic deformation during unloading (E-F). Similar to the previous cycle, the B2→R→B19′ phase transition occurs during loading (D-E), with the reversed transition during unloading (E-F). After unloading, the residual B19′ phase remains (point F), primarily due to plastic deformation of the BCC phase hindering the B19′ phase's reverse transformation. Fig. 5c depicts lattice strain versus macro-strain for the BCC and B2 phases during cyclic loading. Residual stress persists in both phases post-unloading. A negative lattice strain reflects tensile stress, whereas a positive value indicates compressive stress. Specifically, after unloading at different stages, we find that the BCC phase exhibits lattice strains of −0.037 % (at point B), −0.131 % (at point D), and −0.199 % (at point F), respectively. In contrast, the B2 phase displays lattice strains of 0.035 % (at point B), 0.059 % (at point D), and 0.093 % (at point F), respectively. These observations imply that tensile stress persists in the BCC phase after unloading, while the B2 phase maintains compressive stress. With an increasing number of cycles, residual stress becomes more pronounced. In the BCC phase, tensile stress partially counteracts the applied compressive stress during subsequent loading, enhancing the elastic strain limit, reaching 3.2 % during the third unloading. It is worth noting that the BCC phase remains elastic at

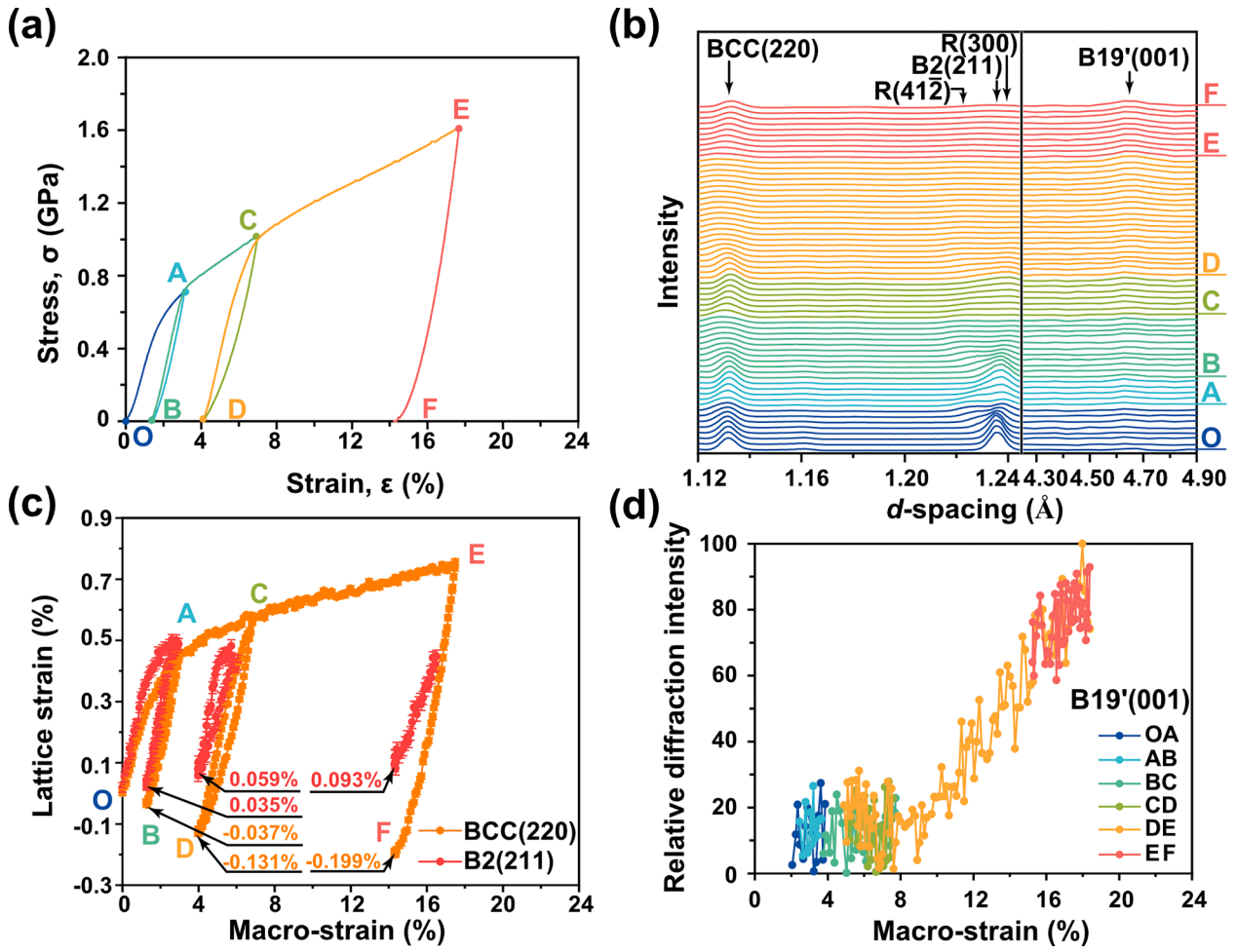

Fig. 5. Deformation mechanisms during cyclic loading. (a) Schematic depiction of the cyclic loading process **(b)** *In-situ* synchrotron high-energy X-ray diffraction patterns recorded during cyclic loading. **(c)** The evolution of lattice strain for BCC (220) and B2 (211) planes during cyclic loading, with analysis data acquired parallel to the loading direction. **(d)** The evolution of the relative diffraction intensity of B19′ (001) peaks during cyclic loading. An inset offers a schematic depiction of the cyclic loading process.

macro-stresses below 1 GPa during stages D-E of the cyclic loading process (**Supplementary Figure 12**). As stress increases, the BCC phase undergoes plastic deformation, transferring the stress to the B2 or B19′ phase. Furthermore, for reversible phase transformations, the B2⇌R transformation primarily occurs at low strain (< 6.7 %), while the B2⇌B19′ transformation mainly takes place at high strain (> 6.7 %) (Fig. 5d). Plastic deformation induced by the BCC phase at elevated strain levels impedes the B19′→R→B2 phase transition during unloading, resulting in a substantial 60 % residual presence of B19′ post-unloading.

We present a schematic representation of the deformation mechanisms in $Ni_{40}Ti_{40}(NbMoTaW)_{20}$ during continuous and cyclic loading

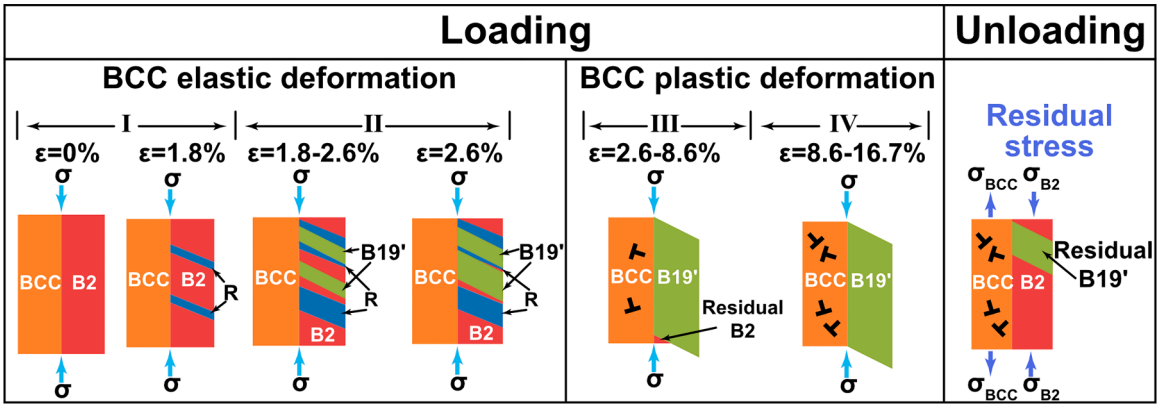

Fig. 6. Schematic representation of the deformation processes during continuous and cyclic loading. A schematic representation elucidating the elastic-plastic deformation within the BCC phase and the phase transition in the B2 matrix. Here, σ represents the external stress; σ_{BCC} symbolizes the microscopic stress on the BCC phase after unloading, and σ_{B2} denotes the microscopic stress on the B2 matrix after unloading.

processes (Fig. 6). During the loading process, in stage I (ε=0 %−1.8 %), the material undergoes the B2→R transformation within the B2 phase, concurrently experiencing elastic strain in both the untransformed B2 and BCC phases. In stage II (ε=1.8 %−2.6 %), R→B19′ and B2→B19′ transitions take place. The untransformed B2 and BCC phases continue their elastic deformation. Progressing to stage III (ε=2.6 %−8.6 %), the B19′ phase fraction increases with strain, with the B19′ phase initially undergoing elastic deformation, followed by plastic deformation. The BCC phase and the residual B2 phase undergo plastic deformation during this stage. In stage IV (ε=8.6 %−16.7 %), plastic deformation occurs in both the B19′ and BCC phases, culminating in the transformation of the residual B2 phase into the B19′ phase. During unloading, the B19′→B2 transformation takes place. After unloading, the BCC phase experiences microscopic tensile stress, while the B2 phase incurs microscopic compressive stress. Therefore, in $Ni_{40}Ti_{40}(NbMoTaW)_{20}$ composite, the B2 NiTi matrix seamlessly integrates with the BCC phase, ensuring exceptional mechanical performance and recoverable strain capacity.

We harness the HEA concept to craft an inventive $Ni_{40}Ti_{40}(NbMoTaW)_{20}$ composite, uniting exceptional strength, ductility, and recoverable strain. Refractory HEAs inherently feature elevated intrinsic strength and pronounced lattice distortion [19,65,66], both pivotal in achieving the high strength observed in the $Ni_{40}Ti_{40}(NbMoTaW)_{20}$ composite. Additionally, within our $Ni_{40}Ti_{40}(NbMoTaW)_{20}$ composite, the BCC phase exhibits a high ideal configurational entropy (**Supplementary Table 1**). The high configurational entropy fosters the formation of a stable BCC solid solution phase [67], eliminating competing intermetallic compounds within the composite matrix. Thus, in $Ni_{40}Ti_{40}(NbMoTaW)_{20}$, the fraction of the brittle Ti_2Ni phase is minimized. This reduction significantly enhances the ductility of the $Ni_{40}Ti_{40}(NbMoTaW)_{20}$ composite (Fig. 1a). Furthermore, during loading, the BCC phase exhibits a substantial elastic strain of 2.7 % (Fig. 4b), attributed to the effect of lattice strain matching between the transformation lattice distortion of the B2 NiTi matrix and the elastic strain of the BCC phase [68]. These unique micromechanical characteristics further underpin the high strength and large ductility of $Ni_{40}Ti_{40}(NbMoTaW)_{20}$. Plastic deformation generates crystallographic defects such as dislocations, which permanently cause strain in the material. As dislocations accumulate, irreversible strain grows, while reversible strain diminishes. Moreover, multiple-element doping induces a multi-step phase transition process in $Ni_{40}Ti_{40}(NbMoTaW)_{20}$ composite, prompting the occurrence of the B2→R→B19′ phase transition during continuous loading and the B2⇌R⇌B19′ phase transition during cyclic loading. Consequently, the combination of lattice strain matching and the reversible B2⇌R⇌B19′ phase transition plays a pivotal role in imparting $Ni_{40}Ti_{40}(NbMoTaW)_{20}$ with its remarkable ductility and substantial recoverable strain. Meanwhile, the low Young's modulus and high strength of the composite also contribute to the enhanced recoverable strain. Importantly, the extensive compositional flexibility of HEAs, coupled with the manifold advantages stemming from the aforementioned structural features, markedly expands the design landscape for NiTi-based composites. This boundless potential facilitates the development of innovative NiTi-based composites that seamlessly integrate a range of exceptional properties into a unified whole.

4. Conclusion

In summary, we pioneer the utilization of the HEA concept in the fabrication of NiTi-based composites. The developed composite is primarily composed of a B2 NiTi matrix and a BCC compositionally complex phase. Importantly, the composite exhibits remarkable attributes, featuring exceptional strength, large ductility, and a superb recoverable strain capacity. Notably, it showcases an engineering compressive strength of 3274 MPa, accompanied by a compressive fracture strain of 44.2 % and a maximum recoverable strain of 7.3 %. The extraordinary mechanical performance is attributed to the unique structural characteristics of the compositionally complex phase and the lattice strain matching induced by phase transitions. Furthermore, multi-element microalloying within the B2 phase introduces a reversible B2⇌R⇌B19′ phase transition process, resulting in a significant recoverable strain. As a result, the crystallographic distortion undergoes a multi-step release, reducing localized stress and crystallographic defects. Additionally, the low Young's modulus and high strength of the composite contribute to its recoverable strain. The combination of lattice strain matching, the reversible B2⇌R⇌B19′ phase transition, and low Young's modulus imparts $Ni_{40}Ti_{40}(NbMoTaW)_{20}$ with remarkable ductility and substantial recoverable strain. This work not only introduces a novel category of NiTi-based composites but also offers valuable insights into strategies for enhancing their performance through the HEA concept.

CRediT authorship contribution statement

Jiayi Geng: Writing – original draft, Visualization, Methodology, Investigation, Formal analysis, Data curation. **Yunzhu Shi:** Writing – review & editing, Supervision, Funding acquisition, Conceptualization. **Pere Barriobero-Vila:** Resources, Methodology, Investigation, Data curation. **Meiyuan Jiao:** Resources, Methodology, Data curation. **Yihuan Cao:** Resources, Methodology, Investigation. **Yu Tang:** Resources, Methodology, Investigation, Data curation. **Jingzhi He:** Methodology, Investigation, Data curation. **Chao Ma:** Resources, Methodology, Investigation. **Yan Ma:** Resources, Methodology, Investigation. **Zhifeng Lei:** Writing – review & editing, Validation, Supervision, Project administration, Funding acquisition, Conceptualization. **Zhaoping Lu:** Writing – review & editing, Supervision, Conceptualization.

Declaration of competing interest

The authors declare that they have no known competing financial interests or personal relationships that could have appeared to influence the work reported in this paper.

Data availability

Data will be made available on request.

Acknowledgments

This research was funded by the National Natural Science Foundation of China (Nos. 52371153, 52101194), the Natural Science Foundation of Hunan Province (No. 2022JJ40078), The Fundamental Research Funds for the Central Universities (Nos. 531118010621, 531118010671) and The Science and Technology Innovation Program of Hunan Province (No. 2022RC1083). The authors would like to acknowledge the support provided by A. Stark and N. Schell (Helmholtz-Zentrum Hereon) for the diffraction experiments performed at the P07-HEMS beamline. The Deutsches Elektronen-Synchrotron (DESY) is acknowledged for the provision of synchrotron radiation facilities in the framework of the proposal I-20221372 EC. P.B.V. acknowledges financial support from the Spanish Ministry of Science through the Ramón y Cajal grant RYC2020–029585-I.

Supplementary materials

Supplementary material associated with this article can be found, in the online version, at doi:10.1016/j.apmt.2024.102347.

References

[1] S. Hao, L. Cui, D. Jiang, X. Han, Y. Ren, J. Jiang, Y. Liu, Z. Liu, S. Mao, Y. Wang, Y. Li, X. Ren, X. Ding, S. Wang, C. Yu, X. Shi, M. Du, F. Yang, Y. Zheng, Z. Zhang, X. Li, D.E. Brown, J. Li, A transforming metal nanocomposite with large elastic strain, low modulus, and high strength, Science 339 (2013) 1191–1194, https://doi.org/10.1126/science.1228602.

[2] E. Farber, J.-N. Zhu, A. Popovich, V. Popovich, A review of NiTi shape memory alloy as a smart material produced by additive manufacturing, Mater. Today Proc 30 (2020) 761–767, https://doi.org/10.1016/j.matpr.2020.01.563.

[3] J. Mohd Jani, M. Leary, A. Subic, M.A. Gibson, A review of shape memory alloy research, applications and opportunities, Mater. Des. 1980-2015 56 (2014) 1078–1113, https://doi.org/10.1016/j.matdes.2013.11.084.

[4] S.K. Patel, B. Behera, B. Swain, R. Roshan, D. Sahoo, A. Behera, A review on NiTi alloys for biomedical applications and their biocompatibility, Mater. Today Proc 33 (2020) 5548–5551, https://doi.org/10.1016/j.matpr.2020.03.538.

[5] J. Zhang, L. Cui, D. Jiang, Y. Liu, S. Hao, Y. Ren, X. Han, Z. Liu, Y. Wang, C. Yu, Y. Huan, X. Zhao, Y. Zheng, H. Xu, X. Ren, X. Li, A biopolymer-like metal enabled hybrid material with exceptional mechanical prowess, Sci. Rep. 5 (2015) 8357, https://doi.org/10.1038/srep08357.

[6] K. Otsuka, X. Ren, Physical metallurgy of Ti–Ni-based shape memory alloys, Prog. Mater. Sci. 50 (2005) 511–678, https://doi.org/10.1016/j.pmatsci.2004.10.001.

[7] F. Guo, S. Hao, X. Jiang, D. Jiang, L. Cui, Y. Ren, Achieving ultra-high bearing strength of tungsten nanoribbons in a transforming metal matrix, J. Alloys Compd. 781 (2019) 1–7, https://doi.org/10.1016/j.jallcom.2018.11.363.

[8] X. Yao, W. Tang, Z. Sun, X. Shi, Y. Wang, Y. Li, J. Jiang, J. Zhang, Effect of NiTi matrix grain size on the ultra-large elastic deformation of V nanowires in a V/NiTi composite, Mater. Today Commun. 29 (2021) 102779, https://doi.org/10.1016/j.mtcomm.2021.102779.

[9] J. Jiang, D. Jiang, S. Hao, C. Yu, J. Zhang, Y. Ren, D. Lu, S. Xie, L. Cui, A nano lamella NbTi–NiTi composite with high strength, Mater. Sci. Eng. A 633 (2015) 121–124, https://doi.org/10.1016/j.msea.2015.03.010.

[10] D. Jiang, S. Hao, J. Zhang, Y. Liu, Y. Ren, L. Cui, In situ synchrotron investigation of the deformation behavior of nanolamellar Ti5Si3/TiNi composite, Scr. Mater. 78–79 (2014) 53–56, https://doi.org/10.1016/j.scriptamat.2014.01.034.

[11] Y. Li, J. Zhang, M. Saunders, Y. Ren, H. Yang, Y. Liu, Martensitic phase transformation induced large elastic lattice strains in Nb3Sn lamellae in NiTi–Nb3Sn eutectic composite, Mater. Sci. Eng. A 866 (2023) 144672, https://doi.org/10.1016/j.msea.2023.144672.

[12] B. Cantor, I.T.H. Chang, P. Knight, A.J.B. Vincent, Microstructural development in equiatomic multicomponent alloys, Mater. Sci. Eng. A 375–377 (2004) 213–218, https://doi.org/10.1016/j.msea.2003.10.257.

[13] J.-W. Yeh, S.-K. Chen, S.-J. Lin, J.-Y. Gan, T.-S. Chin, T.-T. Shun, C.-H. Tsau, S.-Y. Chang, Nanostructured high-entropy alloys with multiple principal elements: novel alloy design concepts and outcomes, Adv. Eng. Mater. 6 (2004) 299–303, https://doi.org/10.1002/adem.200300567.

[14] E.P. George, D. Raabe, R.O. Ritchie, High-entropy alloys, Nat. Rev. Mater. 4 (2019) 515–534, https://doi.org/10.1038/s41578-019-0121-4.

[15] Z. Lei, Y. Wu, J. He, X. Liu, H. Wang, S. Jiang, L. Gu, Q. Zhang, B. Gault, D. Raabe, Z. Lu, Snoek-type damping performance in strong and ductile high-entropy alloys, Sci. Adv. 6 (2020) eaba7802, https://doi.org/10.1126/sciadv.aba7802.

[16] C. Lee, G. Song, M.C. Gao, R. Feng, P. Chen, J. Brechtl, Y. Chen, K. An, W. Guo, J. D. Poplawsky, S. Li, A.T. Samaei, W. Chen, A. Hu, H. Choo, P.K. Liaw, Lattice distortion in a strong and ductile refractory high-entropy alloy, Acta Mater 160 (2018) 158–172, https://doi.org/10.1016/j.actamat.2018.08.053.

[17] D.B. Miracle, O.N. Senkov, A critical review of high entropy alloys and related concepts, Acta Mater 122 (2017) 448–511, https://doi.org/10.1016/j.actamat.2016.08.081.

[18] Y.F. Ye, Q. Wang, J. Lu, C.T. Liu, Y. Yang, High-entropy alloy: challenges and prospects, Mater. Today 19 (2016) 349–362, https://doi.org/10.1016/j.mattod.2015.11.026.

[19] C. Lee, Y. Chou, G. Kim, M.C. Gao, K. An, J. Brechtl, C. Zhang, W. Chen, J. D. Poplawsky, G. Song, Y. Ren, Y. Chou, P.K. Liaw, Lattice-distortion-enhanced yield strength in a refractory high-entropy alloy, Adv. Mater. 32 (2020) 2004029, https://doi.org/10.1002/adma.202004029.

[20] Q.F. He, J.G. Wang, H.A. Chen, Z.Y. Ding, Z.Q. Zhou, L.H. Xiong, J.H. Luan, J. M. Pelletier, J.C. Qiao, Q. Wang, L.L. Fan, Y. Ren, Q.S. Zeng, C.T. Liu, C.W. Pao, D. J. Srolovitz, Y. Yang, A highly distorted ultraelastic chemically complex Elinvar alloy, Nature 602 (2022) 251–257, https://doi.org/10.1038/s41586-021-04309-1.

[21] Z. Lei, X. Liu, Y. Wu, H. Wang, S. Jiang, S. Wang, X. Hui, Y. Wu, B. Gault, P. Kontis, D. Raabe, L. Gu, Q. Zhang, H. Chen, H. Wang, J. Liu, K. An, Q. Zeng, T.-G. Nieh, Z. Lu, Enhanced strength and ductility in a high-entropy alloy via ordered oxygen complexes, Nature 563 (2018) 546–550, https://doi.org/10.1038/s41586-018-0685-y.

[22] Q. Ding, Y. Zhang, X. Chen, X. Fu, D. Chen, S. Chen, L. Gu, F. Wei, H. Bei, Y. Gao, M. Wen, J. Li, Z. Zhang, T. Zhu, R.O. Ritchie, Q. Yu, Tuning element distribution, structure and properties by composition in high-entropy alloys, Nature 574 (2019) 223–227, https://doi.org/10.1038/s41586-019-1617-1.

[23] X. Chen, Q. Wang, Z. Cheng, M. Zhu, H. Zhou, P. Jiang, L. Zhou, Q. Xue, F. Yuan, J. Zhu, X. Wu, E. Ma, Direct observation of chemical short-range order in a medium-entropy alloy, Nature 592 (2021) 712–716, https://doi.org/10.1038/s41586-021-03428-z.

[24] R. Zhang, S. Zhao, J. Ding, Y. Chong, T. Jia, C. Ophus, M. Asta, R.O. Ritchie, A. M. Minor, Short-range order and its impact on the CrCoNi medium-entropy alloy, Nature 581 (2020) 283–287, https://doi.org/10.1038/s41586-020-2275-z.

[25] L. Wang, J. Ding, S. Chen, K. Jin, Q. Zhang, J. Cui, B. Wang, B. Chen, T. Li, Y. Ren, S. Zheng, K. Ming, W. Lu, J. Hou, G. Sha, J. Liang, L. Wang, Y. Xue, E. Ma, Tailoring planar slip to achieve pure metal-like ductility in body-centred-cubic multi-principal element alloys, Nat. Mater. 22 (2023) 950–957, https://doi.org/10.1038/s41563-023-01517-0.

[26] S. Chen, Z.H. Aitken, S. Pattamatta, Z. Wu, Z.G. Yu, D.J. Srolovitz, P.K. Liaw, Y.-W. Zhang, Simultaneously enhancing the ultimate strength and ductility of high-entropy alloys via short-range ordering, Nat. Commun. 12 (2021) 4953, https://doi.org/10.1038/s41467-021-25264-5.

[27] P. Staron, T. Fischer, T. Lippmann, A. Stark, S. Daneshpour, D. Schnubel, E. Uhlmann, R. Gerstenberger, B. Camin, W. Reimers, E. Eidenberger, H. Clemens, N. Huber, A. Schreyer, Situ experiments with synchrotron high-energy X-rays and neutrons, Adv. Eng. Mater 13 (2011) 658–663, https://doi.org/10.1002/adem.201000297.

[28] N. Schell, A. King, F. Beckmann, T. Fischer, M. Müller, A. Schreyer, The high energy materials science beamline (HEMS) at PETRA III, Mater. Sci. Forum 772 (2013) 57–61, https://doi.org/10.4028/www.scientific.net/MSF.772.57.

[29] P. Barriobero-Vila, J. Gussone, K. Kelm, J. Haubrich, A. Stark, N. Schell, G. Requena, An in situ investigation of the deformation mechanisms in a β-quenched Ti-5Al-5V-5Mo-3Cr alloy, Mater. Sci. Eng. A 717 (2018) 134–143, https://doi.org/10.1016/j.msea.2018.01.077.

[30] B.H. Toby, R.B. Von Dreele, GSAS-II : the genesis of a modern open-source all purpose crystallography software package, J. Appl. Crystallogr. 46 (2013) 544–549, https://doi.org/10.1107/S0021889813003531.

[31] Y. Chen, O. Molnárová, O. Tyc, L. Kadeřávek, L. Heller, P. Šittner, Recoverability of large strains and deformation twinning in martensite during tensile deformation of NiTi shape memory alloy polycrystals, Acta Mater 180 (2019) 243–259, https://doi.org/10.1016/j.actamat.2019.09.012.

[32] Y. Wen, Y.-F. Wang, H. Ran, W. Wei, J.-M. Zhang, C.-X. Huang, Improving the mechanical and tribological properties of NiTi alloys by combining cryo-rolling and post-annealing, Acta Metall. Sin. Engl. Lett. 35 (2022) 317–325, https://doi.org/10.1007/s40195-021-01253-x.

[33] W. Guo, H. Kato, Development of a high-damping NiTi shape-memory-alloy-based composite, Mater. Lett. 158 (2015) 1–4, https://doi.org/10.1016/j.matlet.2015.05.143.

[34] S.H. Mills, R.D. Noebe, C. Dellacorte, B. Amin-Ahmadi, A.P. Stebner, Development of nickel-rich nickel–titanium–hafnium alloys for tribological applications, Shape Mem. Superelasticity 6 (2020) 311–322, https://doi.org/10.1007/s40830-020-00296-w.

[35] E. Wang, F. Kang, H. Wang, Y. Cao, F. Jiang, Fabrication, microstructure and mechanical properties of novel NiTi/(Al3Ti + Al3Ni) laminated composites, J. Alloys Compd. 775 (2019) 1307–1315, https://doi.org/10.1016/j.jallcom.2018.10.277.

[36] Y. Zhang, J. Liu, L. Wang, D. Wei, C. Liu, K. Wang, Y. Tang, L. Zhang, W. Lu, Porous NiTiNb alloys with superior strength and ductility induced by modulating eutectic microregion, Acta Mater 239 (2022) 118295, https://doi.org/10.1016/j.actamat.2022.118295.

[37] S. Wisutmethangoon, N. Denmud, L. Sikong, Characteristics and compressive properties of porous NiTi alloy synthesized by SHS technique, Mater. Sci. Eng. A 515 (2009) 93–97, https://doi.org/10.1016/j.msea.2009.02.055.

[38] Y.-H. Li, L.-J. Rong, Y.-Y. Li, Compressive property of porous NiTi alloy synthesized by combustion synthesis, J. Alloys Compd. 345 (2002) 271–274, https://doi.org/10.1016/S0925-8388(02)00412-7.

[39] Y. Qiu, M.L. Young, X. Nie, High strain rate compression of martensitic NiTi shape memory alloys, Shape Mem. Superelasticity 1 (2015) 310–318, https://doi.org/10.1007/s40830-015-0035-y.

[40] P. Hua, M. Xia, Y. Onuki, Q. Sun, Nanocomposite NiTi shape memory alloy with high strength and fatigue resistance, Nat. Nanotechnol. 16 (2021) 409–413, https://doi.org/10.1038/s41565-020-00837-5.

[41] S. Xiaoyun, L. Yan, Z. Fei, L. Shusuo, NiTiAl intermetallic alloys strengthened by Mo replacement, Chin. J. Aeronaut. 23 (2010) 715–719, https://doi.org/10.1016/S1000-9361(09)60274-0.

[42] A.J. Neurohr, D.C. Dunand, Shape-memory NiTi with two-dimensional networks of micro-channels, Acta Biomater 7 (2011) 1862–1872, https://doi.org/10.1016/j.actbio.2010.11.038.

[43] M. Morakabati, Sh. Kheirandish, M. Aboutalebi, A.K. Taheri, S.M. Abbasi, The effect of Cu addition on the hot deformation behavior of NiTi shape memory alloys, J. Alloys Compd. 499 (2010) 57–62, https://doi.org/10.1016/j.jallcom.2010.01.124.

[44] R. Xi, H. Jiang, G. Li, Z. Zhang, G. Zhao, K. Vanmeensel, S. Kustov, J. Van Humbeeck, X. Wang, Effect of Fe addition on the microstructure, transformation behaviour and superelasticity of NiTi alloys fabricated by laser powder bed fusion, Virtual Phys. Prototyp. 18 (2023) e2126376, https://doi.org/10.1080/17452759.2022.2126376.

[45] Y. Koizumi, Y. Ro, S. Nakazawa, H. Harada, NiTi-base intermetallic alloys strengthened by A1 substitution, Mater. Sci. Eng. A 223 (1997) 36–41, https://doi.org/10.1016/S0921-5093(96)10508-6.

[46] M. Zhang, Q. Yu, Z. Liu, J. Zhang, G. Tan, D. Jiao, W. Zhu, S. Li, Z. Zhang, R. Yang, R.O. Ritchie, 3D printed Mg-NiTi interpenetrating-phase composites with high strength, damping capacity, and energy absorption efficiency, Sci. Adv. 6 (2020) eaba5581, https://doi.org/10.1126/sciadv.aba5581.

[47] F. Guo, H. Shen, Z. Xiong, Y. Yang, X. Tong, Y. Guo, S. Hao, Selective laser melting of 60NiTi alloy with superior wear resistance, Metals (Basel) 12 (2022) 620, https://doi.org/10.3390/met12040620.

[48] J. Zhang, Y. Liu, Y. Ren, Y. Huan, S. Hao, C. Yu, Y. Shao, Y. Ru, D. Jiang, L. Cui, In situ synchrotron X-ray diffraction study of deformation behavior and load transfer

in a Ti 2 Ni-NiTi composite, Appl. Phys. Lett. 105 (2014) 041910, https://doi.org/10.1063/1.4892352.
[49] S. Parvizi, S.M. Hashemi, F. Asgarinia, M. Nematollahi, M. Elahinia, Effective parameters on the final properties of NiTi-based alloys manufactured by powder metallurgy methods: a review, Prog. Mater. Sci. 117 (2021) 100739, https://doi.org/10.1016/j.pmatsci.2020.100739.
[50] C. Bewerse, L.C. Brinson, D.C. Dunand, Microstructure and mechanical properties of as-cast quasibinary NiTi–Nb eutectic alloy, Mater. Sci. Eng. A 627 (2015) 360–368, https://doi.org/10.1016/j.msea.2014.12.090.
[51] H. Kato, S. Fukushima, K. Sasaki, Shape Memory Effect and Superelasticity of Textured Niti Alloy Wire, 73, Springer, Cham, 2017, pp. 43–50, https://doi.org/10.1007/978-3-319-53306-3_4.
[52] N. Shayesteh Moghaddam, S. Saedi, A. Amerinatanzi, A. Hinojos, A. Ramazani, J. Kundin, M.J. Mills, H. Karaca, M. Elahinia, Achieving superelasticity in additively manufactured NiTi in compression without post-process heat treatment, Sci. Rep. 9 (2019) 41, https://doi.org/10.1038/s41598-018-36641-4.
[53] X. Hu, Y. Liu, F. Guo, K. Yu, D. Jiang, Y. Ren, H. Yang, L. Cui, Enhanced superelasticity of nanocrystalline NiTi/NiTiNbFe laminar composite, J. Alloys Compd. 853 (2021) 157309, https://doi.org/10.1016/j.jallcom.2020.157309.
[54] O. Benafan, D.J. Gaydosh, R.D. Noebe, S. Qiu, R. Vaidyanathan, In situ neutron diffraction study of NiTi–21Pt high-temperature shape memory alloys, Shape Mem. Superelasticity 2 (2016) 337–346, https://doi.org/10.1007/s40830-016-0095-7.
[55] Q. Yang, J. Chen, S. Zhang, J. Ge, Y. Zhang, S. Huang, X. Wang, Tailoring hardness gradient in Ni50.3Ti29.7Hf20 high temperature shape memory alloy through thermal treatment, Mater. Sci. Eng. -Struct. Mater. Prop. Microstruct. Process. 787 (2020) 139518, https://doi.org/10.1016/j.msea.2020.139518.
[56] J. Zhang, S. Hao, D. Jiang, Y. Huan, L. Cui, Y. Liu, H. Yang, Y. Ren, In situ synchrotron high-energy X-ray diffraction study of microscopic deformation behavior of a hard-soft dual phase composite containing phase transforming matrix, Acta Mater 130 (2017) 297–309, https://doi.org/10.1016/j.actamat.2017.03.052.
[57] S. Liu, W. Liu, J. Liu, J. Liu, L. Zhang, Y. Tang, L.-C. Zhang, L. Wang, Compressive properties and microstructure evolution in NiTiNb alloy with mesh eutectic phase, Mater. Sci. Eng. A 801 (2021) 140434, https://doi.org/10.1016/j.msea.2020.140434.
[58] J.W. Yeh, Y.L. Chen, S.J. Lin, S.K. Chen, High-entropy alloys – a new era of exploitation, Mater. Sci. Forum 560 (2007) 1–9, https://doi.org/10.4028/www.scientific.net/MSF.560.1.
[59] H. Shi, J. Frenzel, G.T. Martinez, S. Van Rompaey, A. Bakulin, S. Kulkova, S. Van Aert, D. Schryvers, Site occupation of Nb atoms in ternary Ni–Ti–Nb shape memory alloys, Acta Mater 74 (2014) 85–95, https://doi.org/10.1016/j.actamat.2014.03.062.
[60] X.B. Wang, B. Verlinden, J. Van Humbeeck, R-phase transformation in NiTi alloys, Mater. Sci. Technol. 30 (2014) 1517–1529, https://doi.org/10.1179/1743284714Y.0000000590.
[61] S. Miyazaki, S. Kimura, K. Otsuka, Shape-memory effect and pseudoelasticity associated with the R-phase transition in Ti-50·5 at.% Ni single crystals, Philos. Mag. A 57 (1988) 467–478, https://doi.org/10.1080/01418618808204680.
[62] B. Li, Y. Shen, Q. An, Structural origin of reversible martensitic transformation and reversible twinning in NiTi shape memory alloy, Acta Mater 199 (2020) 240–252, https://doi.org/10.1016/j.actamat.2020.08.039.
[63] D. Wang, Z. Zhang, J. Zhang, Y. Zhou, Y. Wang, X. Ding, Y. Wang, X. Ren, Strain glass in Fe-doped Ti–Ni, Acta Mater 58 (2010) 6206–6215, https://doi.org/10.1016/j.actamat.2010.07.040.
[64] D.D. Johnson, P. Singh, A.V. Smirnov, N. Argibay, Universal maximum strength of solid metals and alloys, Phys. Rev. Lett. 130 (2023) 166101, https://doi.org/10.1103/PhysRevLett.130.166101.
[65] Y. Zou, H. Ma, R. Spolenak, Ultrastrong ductile and stable high-entropy alloys at small scales, Nat. Commun. 6 (2015) 7748, https://doi.org/10.1038/ncomms8748.
[66] F. Wang, G.H. Balbus, S. Xu, Y. Su, J. Shin, P.F. Rottmann, K.E. Knipling, J.-C. Stinville, L.H. Mills, O.N. Senkov, I.J. Beyerlein, T.M. Pollock, D.S. Gianola, Multiplicity of dislocation pathways in a refractory multiprincipal element alloy, Science 370 (2020) 95–101, https://doi.org/10.1126/science.aba3722.
[67] O.N. Senkov, D.B. Miracle, K.J. Chaput, J.-P. Couzinie, Development and exploration of refractory high entropy alloys—a review, J. Mater. Res. 33 (2018) 3092–3128, https://doi.org/10.1557/jmr.2018.153.
[68] J. Zhang, Y. Liu, L. Cui, S. Hao, D. Jiang, K. Yu, S. Mao, Y. Ren, H. Yang, "Lattice strain matching"-enabled nanocomposite design to harness the exceptional mechanical properties of nanomaterials in bulk forms, Adv. Mater. 32 (2020) 1904387, https://doi.org/10.1002/adma.201904387.